# Stabilization of Rock Salt ZnO Nanocrystals by Low-Energy Surfaces and Mg Additions: A First-Principles Study

Rik S. Koster,* Changming M. Fang, Marjolein Dijkstra, Alfons van Blaaderen, and Marijn A. van Huis*

Soft Condensed Matter, Debye Institute for Nanomaterials Science, Utrecht University, Princetonplein 5, 3584 CC Utrecht, The Netherlands

S *Supporting Information*

ABSTRACT: Whereas bulk zinc oxide (ZnO) exhibits the wurtzite crystal structure, nanoscale ZnO was recently synthesized in the rock salt structure by addition of Mg. Using first-principles methods, we investigated two stabilization routes for accessing rock salt ZnO. The first route is stabilization by Mg addition, which was investigated by considering ZnO–MgO mixed phases. The second route is through size effects, as surface energies become dominant for small nanocrystal sizes. We discovered that the surface energy of rock salt ZnO is surprisingly low at 0.63 J m^{-2}, which is lower than those of wurtzite and zinc blende ZnO and lower than that of rock salt MgO. We predict that pure rock salt ZnO is stable for nanocrystals smaller than 1.6 nm, and that Mg additions can greatly extend the size range in which the rock salt phase is stable. Both mixed-phase and core–shell models were considered in the calculations. The present approach could be applied to predict the stabilization of many other nanocrystal phases in deviating crystal structures.
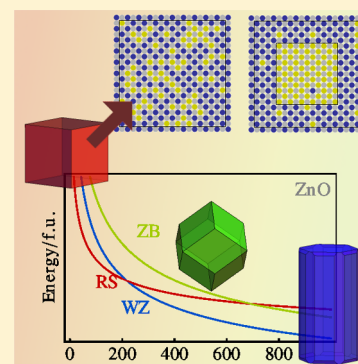
INTRODUCTION

Zinc oxide is an abundantly used II–VI semiconductor nanomaterial, because of its favorable optoelectronic properties. It has a wide band gap of 3.37 eV and a high exciton binding energy of 60 meV. ZnO has many applications in electronics, optics, photovoltaics, and data storage, and it is used in gas sensors and photodetectors.[1–10] Because of this very wide applicability, the properties of bulk and nanoscale ZnO have been intensively investigated, as summarized in several review papers.[1–4] Under ambient conditions, ZnO has the wurtzite (WZ) crystal structure. Nanoparticles of various morphologies, such as nanorods, tetrapods,[11–13] nanowires,[14,15] nanohelices,[16] and microcheerios,[17] have been synthesized. At high pressure, ZnO transforms to a rock salt (RS) structure, a transition that has been well studied, both experimentally[18–20] and theoretically.[21–23]

Zou et al.[24] produced RS ZnO nanocrystals of 1–2-nm size by means of a microemulsion method. They attributed the formation of rock salt ZnO nanocrystals to the chemical bonds between the surface of the particles and the surfactant molecules.[24]

To increase the stability of the RS phase, ZnO can be doped with metals such as Mg, Mn, and Co. First-principles calculations by Zhang et al.[25] and Wang et al.[26] showed that Mn and Co doping decreased the WZ–RS transition pressure. Yang et al. found that the morphology of the obtained nanoparticles depends strongly on the amount of the Mg precursor.[12] The RS phase has also been observed as thin layers, grown on cubic substrates.[27,28] The stability of Mn-doped nanowires was studied by Yan et al.,[29] using both Raman spectroscopy and density functional theory. Ueda et al.[30] found that ZnO films doped with Co can exhibit ferromagnetic

behavior. Chen et al.[31,32] created thin Mg$_x$Zn$_{1-x}$O films with both WZ and RS structures. Limpijumnong et al.[33] studied MgO–ZnO nanocrystal alloys by X-ray absorption near-edge structure (XANES) spectroscopy and found that Zn is highly miscible in RS MgO, whereas Mg is only slightly miscible in WZ ZnO.

In this work, the effect of Mg addition on ZnO nanocrystals was studied by density functional theory (DFT) total energy calculations of Mg$_x$Zn$_{1-x}$O for different values of x to produce the relative stabilities of the wurtzite, rock salt, and zinc blende phases at zero temperature. However, as a first-order attempt to gauge the effects of entropy at finite temperature, we calculated free energies by considering only "ideal" mixing terms. To study the nature of the chemical bonding, Bader charge analysis[34] was performed. Furthermore, surface energies for several low-index surfaces were calculated.

First, we discuss the results of the mixed Mg$_x$Zn$_{1-x}$O bulk phases. Second, surface energies of ZnO and MgO are presented. Third, we discuss the stability of the pure ZnO and MgO nanocrystals, followed by the stability of the mixed Mg$_x$Zn$_{1-x}$O nanocrystals.

COMPUTATIONAL METHODS

For the DFT calculations, the first-principles Vienna Ab Initio Simulation Package[35] (VASP) code was used. For a description of DFT in general, we refer to the original papers of Kohn and Sham.[36–38] The generalized gradient approximation functional of Perdew, Burke, and Ernzerhof[39,40] (GGA-PBE) was used

within the projected augmented wave (PAW) method.[41] A cutoff energy of 600 eV was used for the wave functions, along with a cutoff of 900 eV for the augmentation charges, to ensure energy convergence within 2 meV/atom.

With respect to the density of the k-mesh, convergence was ascertained to well within 2 meV/atom in all cases. For the supercells of the mixed phases, the Γ-centered k-point mesh was set to $7 \times 7 \times 7$, whereas for the surface slabs, the choice of k-mesh varied, because the shapes and sizes varied.

A well-known shortcoming of the GGA functional is an underestimation of the band gap in semiconductors. ZnO is a particularly notorious example of this effect: Our GGA calculation of the band structure of a ZnO conventional unit cell predicts a band gap of 0.73 eV instead of the experimental value of 3.37 eV. This discrepancy can be attributed to the GGA, which was developed for metals and therefore underestimates the binding of the Zn 3d electrons. This leads to increased interactions of these 3d electrons with the electrons in the valence and conduction bands, resulting in a smaller band gap.

One way to reduce this problem is by including a Hubbard U correction term for the Zn 3d electrons, which artificially pushes the d bands down. Unfortunately, the value of this parameter U cannot be derived theoretically and differs from material to material. It is essentially a fit parameter, introduced in a first-principles theory. Other methods to obtain reliable electronic structures, such as hybrid functionals (PBE0, HSE, etc.) or the quasiparticle GW technique, are computationally expensive and therefore cannot be used for the large supercells described in this work. The Hubbard U correction term provides a computationally cheap alternative and was used in all calculations with a value of 5.0 eV. A more elaborate discussion on the Hubbard U value used can be found in the Supporting Information.

To examine the charge distributions among the atoms in the supercells and slabs, Bader[34] charge analysis was performed. This method determines the charge on the atoms unambiguously, by defining the boundary between two atoms at the surface where the gradient of the charge density is zero. The charge within the volume enclosed by this surface is then interpreted as the charge on the atom. To this end, we used the Bader charge analysis code by Henkelman and co-workers.[42−44]

■ RESULTS AND DISCUSSION

Bulk Energies of Rock Salt and Wurtzite Mg$_x$Zn$_{1−x}$O phases. The wurtzite crystal structure has a hexagonal lattice, whereas the conventional unit cells of the rock salt and zinc blende (ZB) crystal structures are cubic. In DFT calculations, comparing results obtained with different lattices can introduce small systematic errors. To reduce such effects, all calculations were done using similar cells. Any crystal structure that is based on the face-centered-cubic (fcc) lattice can be cast into a hexagonal unit cell with $a_{hex} = \frac{1}{2}(2)^{1/2}a_{cub}$ and $c_{hex} = (3)^{1/2}a_{cub}$. Doing this for the RS and ZB structures produces hexagonal unit cells with three Zn/Mg and three O atoms. The wurtzite unit cell has two atoms of each element, so supercells consisting of $3 \times 3 \times 3$ WZ unit cells and supercells consisting of $3 \times 3 \times 2$ hexagonal RS/WZ unit cells are similar in shape and size and contain equal numbers of atoms (108). Using these supercells will therefore reduce possible systematic errors arising from differences in the cells used.

In all of these supercells, the atoms are organized in alternating layers of Mg/Zn and O. The difference between these supercells lies in the stacking of these layers. There are three positions on which the atoms of a layer can be centered: A/a $(0, 0, z)$, B/b $(^1/_3, ^2/_3, z)$, and C/c $(^2/_3, ^1/_3, z)$, where coordinates are expressed in fractions of the lattice vectors. Here, capital letters denote Mg/Zn layers, and lowercase letters denote O layers. The stackings are AaBb... for WZ, AaBbCc... for ZB, and AcBaCb... for RS. In Figure 1, the stackings of the layers in the hexagonal unit cells are shown.
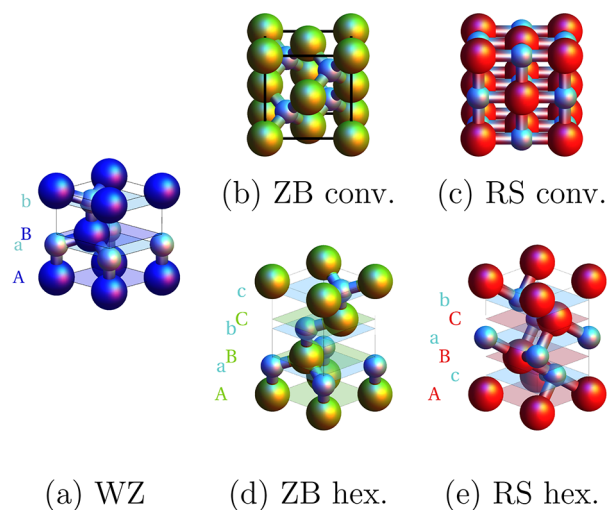
Figure 1. Conventional unit cells and hexagonal unit cells with layer stacking indicated. Supercells used in the calculation consist of $3 \times 3 \times 3$ wurtzite unit cells or $3 \times 3 \times 2$ zinc blende or rock salt hexagonal unit cells.

In each crystal structure, supercells of mixed-phase Mg$_x$Zn$_{1−x}$O for a number of values of the composition x were created by replacing $54x$ of the 54 Zn atoms by Mg atoms, whereby the replacements were distributed over the lattice to obtain randomly mixed configurations. The O sublattice remained unaltered. Total energy calculations were performed, whereby the lattice vectors and the positions of the atoms were allowed to relax. The lattice parameters obtained in these calculations are listed in Table 1 (pure MgO and ZnO) and shown Figure S3 (Supporting Information).

The general formula for the formation energy of a defect is given by[45,46]

$$E_{form} = E_t^d - E_t^p - \sum_i \Delta n_i \mu_i + qE_F \tag{1}$$

Table 1. Lattice Constants

	this work (DFT)	expt[a]
	MgO	
RS	a = 4.237 Å	a = 4.212 Å
ZB	a = 4.598 Å	
WZ	a = 3.310 Å	
	c = 5.082 Å	
	ZnO	
RS	a = 4.261 Å	a = 4.271−4.294 Å
ZB	a = 4.551 Å	a = 4.37−4.47 Å
WZ	a = 3.234 Å	a = 3.2475−3.2501 Å
	c = 5.211 Å	c = 5.2042−5.2075 Å

[a]Experimental data from Özgür et al.[3] and references therein.

whereby E_{form} is the formation energy, E_t^d is the total energy of the defect cell, and E_t^p is the total energy of the perfect cell. Δn_i represents the number of atoms added to or subtracted from the perfect cell, and μ_i represents the chemical potentials for these atoms. q is the charge of the defect, and E_F is the Fermi energy.

This expression simplifies for the calculations described in this article. The possibility of charged defects was not considered in this work, and therefore, $q = 0$ in eq 1, so that the last term vanishes. Moreover, all of our calculations are stoichiometric in the number of cations and anions: $\Delta n_{Mg} = -\Delta n_{Zn}$. Consider a supercell with m MgO and $N-m$ ZnO units. Then, eq 1 becomes

$$E_{form}(Mg_m Zn_{N-m}O_N)$$
$$= E_t^d(Mg_m Zn_{N-m}O_N) - E_t^p(Zn_N O_N) - m\mu_{Mg} + m\mu_{Zn} \quad (2)$$

The chemical potentials are the reservoirs with which atoms are being exchanged, which, in the present work, are the bulk phases of MgO and ZnO. Therefore, $\mu_{Mg} + {}^1\!/_2\mu_{O_2} = E(MgO)$ and $\mu_{Zn} + {}^1\!/_2\mu_{O_2} = E(ZnO)$, and eq 2 can be simplfied to

$$E_{form}(Mg_m Zn_{N-m}O_N)$$
$$= E_t^d(Mg_m Zn_{N-m}O_N) - mE_t^p(MgO)$$
$$- (N - m)E_t^p(ZnO) \quad (3)$$

Dividing by N and relabeling some of the terms provides a simple formula for the formation energy per formula unit, very similar to that used by Liu and Zunger[47]

$$\Delta E(Mg_x Zn_{1-x}O) = E(Mg_x Zn_{1-x}O) - xE_{RS}(MgO)$$
$$- (1 - x)E_{WZ}(ZnO) \quad (4)$$

where all energies are per formula unit $Mg_x Zn_{1-x}O$.

GGA + U calculations are valid for zero pressure and zero temperature, and zero-point vibrational contributions were neglected in this work. Errors in the formation energies due to spurious electrostatic interactions in the finite-size cells[46] were also neglected. Because of these systematic inaccuracies, very small energy differences should be considered as not significant.

By making one cation Mg and all of the others Zn, and vice versa, we obtained the solution energy E^{sol} of MgO in ZnO and vice versa. As reference energies for the pure structures, the energies of the corresponding perfect cells were taken, whereas for the dopant, the energies of the lowest-energy structures were used (i.e., WZ ZnO and RS MgO). The solution energies are listed in Table 2. All solution energies are very low, less than 10 meV in all cases, which is of the same order of magnitude as the systematic errors associated with DFT calculations (choice of exchange-correlation functionals, exclusion of zero-point vibration contributions, etc.). The dissolution of MgO into

Table 2. Solution Energies for the Wurzite and Rock Salt Structures

solution	E^{sol} (meV)
MgO in RS ZnO	−6
ZnO in RS MgO	4
MgO in WZ ZnO	2
ZnO in WZ MgO	−3

ZnO and vice versa is thus not favorable and also not unfavorable. However, this also implies that small pressure and temperature effects can easily stabilize a solid solution.

The formation energy ΔE (as defined in eq 4) is plotted as a function of the parameter x in Figure 2 (top). By definition, ΔE
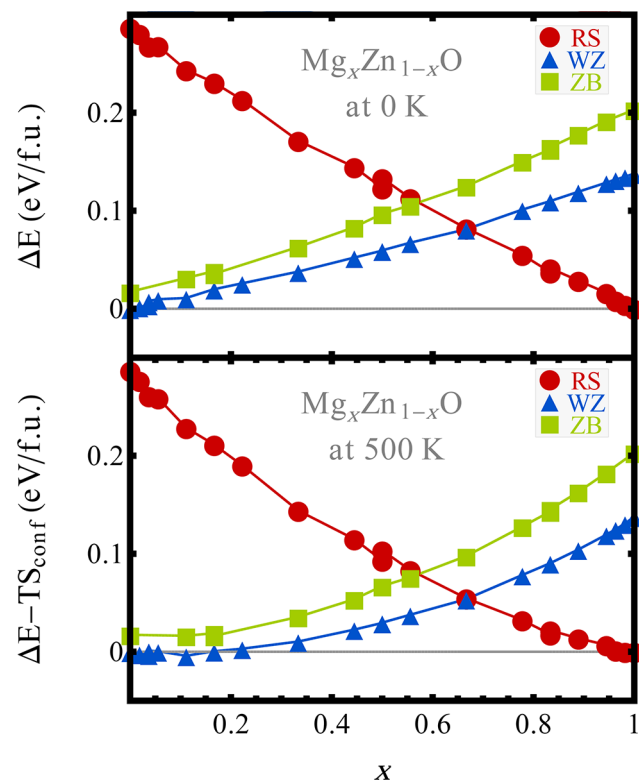
Figure 2. $\Delta E - TS_{conf}$ in electronvolts per formula unit for bulk $Mg_x Zn_{1-x}O$ as a function of x, at temperatures $T = 0$ and 500 K. Lines are drawn to guide the eye.

$= 0$ for WZ ZnO and RS MgO, the known stable structures. All other values of ΔE were found to be positive. For x between 0 and roughly ${}^2\!/_3$, wurzite is the most favorable crystal structure, whereas for ${}^2\!/_3 < x < 1$, rock salt is most stable. The zinc blende phase is unfavorable for any $x > 0$.

The calculations were all performed for a temperature of 0 K and a pressure of 0 GPa. For realistic situations (i.e., at finite temperature), where the Gibbs free energy is the physically relevant quantity, entropy contributions must be taken into account. Here, we restrict ourselves to providing an indication of the effects of entropy by considering ideal mixing entropy contributions. The "ideal" entropy contribution corresponding to mixing Mg and Zn atoms is given by

$$\frac{S_{conf}}{N} = -k_B[x \ln x + (1 - x) \ln(1 - x)] \quad (5)$$

The result of taking this entropy term into account is shown in Figure 2 for temperatures of 0 and 500 K. Where the 0 K graph shows no stable mixed phase, a common-tangent construction in the 500 K figure shows that the wurzite phase can be stable up to a Mg concentration of $x = 0.08$. The rock salt phase also shows some stability under small amounts of Zn doping ($x > 0.99$). This is in contradiction with the results of Limpijumnong et al.,[33] who found that Zn is highly miscible in RS MgO whereas Mg is only slightly miscible in WZ ZnO. Using the common-tangent method, a pseudobinary phase diagram was

constructed (Figure 3). From these phase diagrams, it becomes clear that phase separation is predicted at low temperature and
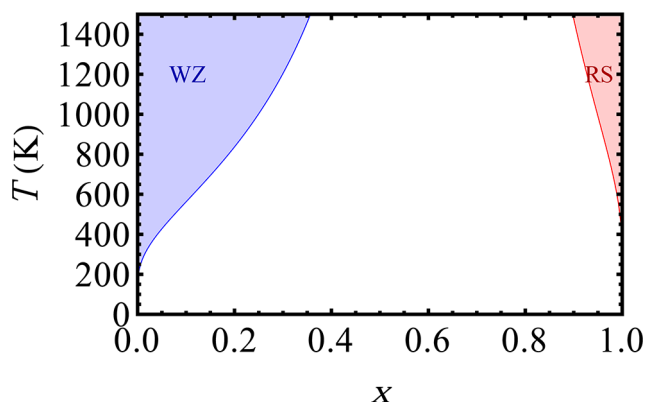

Figure 3. Pseudobinary phase diagram of $Mg_xZn_{1-x}O$.

that taking configurational entropy into account at finite temperatures is not sufficient to explain the experimental observations on rock salt ZnO nanocrystals.

It is also interesting to quantify how the charges on the atoms vary for MgO, ZnO, and the mixed phases. The Bader charges on the atoms as a function of x are shown in Figure 4.
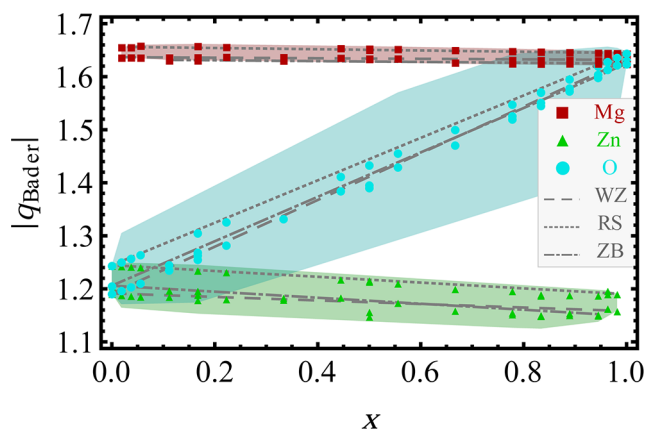

Figure 4. Absolute values of the Bader charges on atoms of $Mg_xZn_{1-x}O$ as a function of x. Values for wurtzite, rock salt, and zinc blende are all plotted. The symbols are averages over all atoms of one type in a cell, whereas shaded areas indicate the ranges in which charges on different atoms of this type can be found.

The average charges on the Mg, Zn, and O atoms vary more or less linearly with x. This change is very small for the cations (~ 0.02 e), and none of the cations within a cell has a charge that deviates much from the average. The average charge on the oxygen atoms, on the other hand, varies from -1.2 e to -1.6 e, and there is considerable variation among the O atoms within a cell. This large variation in the charges on the O atoms within a cell is directly correlated with the local atomic environment of the O atoms. The larger the number of nearest-neighbor Mg cations (or the lower the number of nearest-neighbor Zn cations), the higher the charge on the O atom. This relation can be clearly seen in Figure 5, in which the charge of each atom is compared to the average charge of its nearest neighbors. The nearly vertical lines for the cations indicate that the charges on the cations are barely influenced by the surrounding O atoms, whereas the charges on the O atoms are strongly determined by
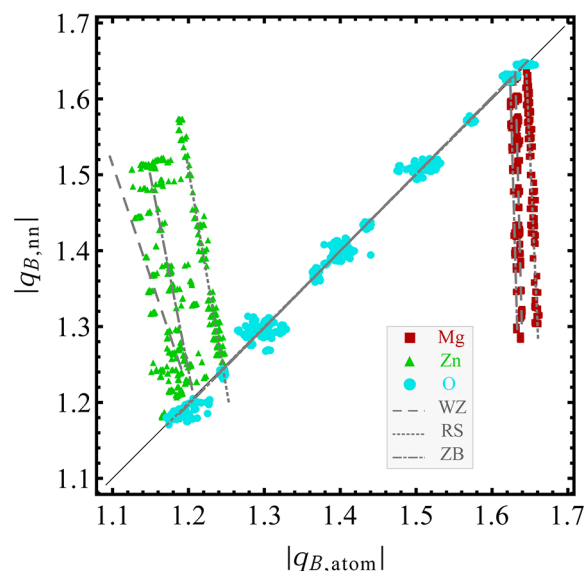

Figure 5. Absolute values of the Bader charges on atoms in $Mg_xZn_{1-x}O$ plotted against the average absolute Bader charge on the nearest-neighbor (nn) atoms. Dashed lines are linear fits for the different crystal structures. Note that the cations follow nearly vertical trends, whereas the oxygen atoms fall on the line $|q_{B,atom}| = |q_{B,nn}|$.

the surrounding cations. The charges on both anions and cations in the RS phase are consistently higher than the charges on the atoms in the ZB and WZ phases, which is most likely due to the fact that, in the RS phase, the number of interactions with neighboring atoms is larger as all atoms are in six-fold coordination in the RS phase whereas all atoms are in four-fold coordination in the ZB and WZ phases. Comparing the different crystal structures, there is little difference in the charges between WZ and ZB, whereas the charges for RS are consistently $0.02-0.04$ e higher.

ZnO and MgO Surface Energies. The DFT calculations on bulk formation energies suggest that, even at finite temperature, RS $Mg_xZn_{1-x}O$ is stable for only small amounts of Zn. Therefore, this effect is not sufficient to explain the rock salt phase found experimentally in Mg-doped ZnO nanocrystals, whereby Mg constitutes less than one-half of the cations.

Because the ZnO rock salt phase has been observed experimentally only at the nanoscale, surface effects are expected to play a major role in stabilizing this phase. For the calculations of the surface energies, finite slabs exposing different facets were constructed. Several low-index surfaces are shown in Figure 6. Figures of the complete slabs used in the calculations can be found in the Supporting Information (Figures S4 and S5).

The slabs were generated using the lattice parameters for bulk MgO and ZnO. The slabs were at least eight layers thick, and a vacuum of at least 20 Å was used. The lattice vectors of these slab supercells were kept fixed, but the positions of the atoms within these slab cells were allowed to relax.

The surface energy of such a slab is given by

$$E_{surface} = \frac{1}{2A}\left(E_{slab} - n_{slab}\frac{E_{bulk}}{n_{bulk}}\right) \tag{6}$$

where E_{slab} and E_{bulk} are the DFT-calculated energies of the slab and bulk (super)cells, respectively, and n_{slab} and n_{bulk} are the corresponding numbers of atoms in these cells. A is the surface area of the slab cell, and the factor of 2 arises from the fact that
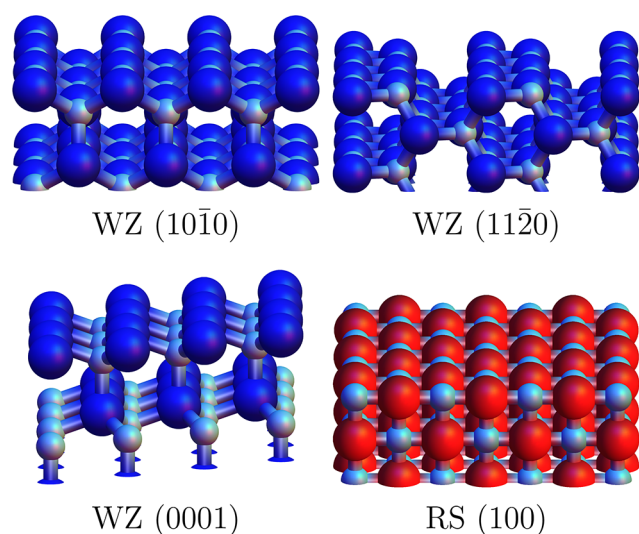
Figure 6. Schematic structures of several low-index surfaces: WZ $(10\bar{1}0)$, $(11\bar{2}0)$, and (0001) in the top left, top right, and bottom left panels, respectively, and RS (001) in the bottom right panel. Light blue indicates oxygen atoms; dark blue, cations in a WZ structure; and red, cations in an RS structure.

Table 3. Surface Energies for the Wurzite, Rock Salt, and Zinc Blende Phases

| crystal structure	surface[b]	$E_{surf}{}^a$ (J/m^2)	
		ZnO[c]	MgO
WZ	$(10\bar{1}0)_{T_1}$	2.56	3.57
	$(10\bar{1}0)_{T_2}$	**0.94**	**1.40**
	$(11\bar{2}0)$	**0.98**	1.45
	$(0001)_{T_3}$	5.57	6.78
	$(0001)_{T_4}$	1.88	2.03
	$(0001)_{T_5}$	2.86	3.72
	$(0001)_{T_6}$	3.06	3.72
	$(10\bar{1}1)_{T_1}$	4.35	4.99
	$(10\bar{1}1)_{T_2}$	4.35	4.99
	$(10\bar{1}1)_{T_3}$	1.66	2.01
	$(10\bar{1}1)_{T_4}$	1.83	2.03
	$(11\bar{2}1)_{T_1}$	1.62	1.86
	$(11\bar{2}1)_{T_2}$	2.12	2.90
RS	(001)	**0.63**	**0.89**
	(011)	1.52	2.17
	$(111)_{T_1}$	1.77	2.90
	$(111)_{T_2}$	1.53	3.00
	$(111)_{T_3}$	3.74	5.63
ZB	(001)	3.91	4.19
	(011)	**1.49**	**1.31**
	$(111)_{T_3}$	6.38	6.68
	$(111)_{T_4}$	3.00	2.45

^{a}Lowest surface energies for each phase marked in bold. ^{b}Different T subscripts denote different terminations. ^{c}Calculations for ZnO done with a Hubbard U correction.

there are two surfaces in the calculation cell. Because DFT surface calculations must always be compared to bulk results, it is not possible to calculate the surface energies of non-stoichiometric slab cells, such as for the polar RS (111) and WZ (0001) surfaces. It is possible to calculate the energies of such slabs with one Zn-/Mg-terminated and one O-terminated surface, but the contributions of the two surfaces cannot be distinguished and an average surface energy is calculated.

Slabs with polar surfaces usually have high energies, because they have dipole moments. This issue can be resolved in two ways: by surface reconstruction or by charge redistribution. For simplicity, we consider only WZ (0001) line reconstructions here. More complicated reconstructions, such as triangular[48] or honeycomb,[49] are not considered. Charge redistribution in the slab using the Bader charge formalism is discussed in more detail in the Supporting Information (Figures S11–S17).

The surface energies obtained are summarized in Table 3. The results for $(10\bar{1}0)$ and $(11\bar{2}0)$ ZnO surfaces are in reasonable agreement with earlier DFT calculations by Spencer et al.[50] and Cooke et al.,[51] but Beltrán et al.[52] and Marana et al.[53] obtained considerably larger values for the surface energies. The ZnO (0001) surface energy is in reasonable agreement with the results found by Wander et al.[54] MgO RS (001) and (011) surface energies are in reasonable agreement with those of Broqvist et al.[55] but are considerably lower than the values obtained by Evarestov and Bandura.[56] We note here that we have considered only bare surfaces, whereas under experimental conditions, the effects of ligands are often of high importance.

We now discuss the structural properties of the surfaces in more detail. The different T subscripts in Table 3 indicate different surface terminations. For example, the wurzite (0001) T_3-terminated surface slab has a polar Zn surface on one end and a polar O surface on the other such that three bonds are broken. The T_4 slab is similar, but only one bond is broken, and therefore, the surface energy of the T_4 slab is considerably less than the surface energy of the T_3 slab. A possible way to reduce surface energies is by reconstruction, for example, by taking one-half of the atoms in the top layer and putting them on the bottom of the slab. In this way, both the upper and lower

surfaces are formed by half-filled layers of the same atom. T_5 and T_6 are slabs with such reconstructed surfaces, both effectively creating lines of Zn (T_5) and O (T_6) on the surfaces. As can be seen from Table 3, the T_4 polar surface actually has a lower surface energy than the reconstructions T_5 and T_6.

From Table 3, two points should be noted. First, the rock salt surface energies of both ZnO and MgO are lower than the wurtzite surface energies. This suggests that, at the nanoscale, the rock salt crystal structure might be favored, in particular when the nanocrystals are small (i.e., when they have a large surface-to-volume ratio). Second, almost all ZnO surface energies are lower than their MgO counterparts, indicating that ZnO surface termination is favored. In particular, the ZnO RS (001) surface energy is very low at 0.63 J m^{-2}.

Stability of Pure ZnO and MgO Nanocrystals. Using the obtained surface energies, the morphologies of pure MgO and pure ZnO nanocrystals can be determined by Wulff construction.[57] This produces cubes for the RS crystal structure, rhombic dodecahedra for the ZB crystal structure, and faceted particles for the WZ crystal structure, as shown in Figure 7. Because the total surface energy scales as $E_{S,tot} \propto A \propto N^{2/3}$, the total energy per formula unit is approximately given by

$$E_{tot,fu}(N) = \frac{E_{tot,part}(N)}{N} = E_{bulk} + E_S N^{-1/3} \tag{7}$$
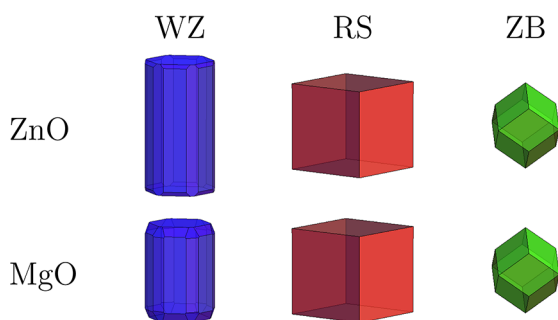
Figure 7. Nanoparticle morphologies of pure ZnO and MgO as predicted by Wulff construction.

where N is the number of MgO or ZnO units and E_S is a weighted sum over surface energies present in the Wulff construction. We mention here that the energy associated with the formation of edges and corners is neglected. In Figure 8,
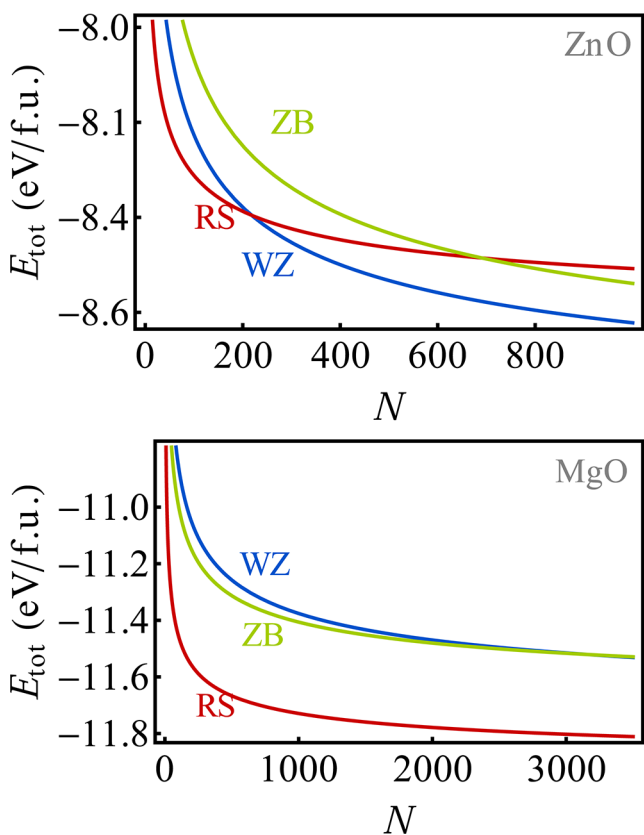

Figure 8. Total energy (electronvolts per formula unit) as defined in eq 7 for ZnO nanocrystals (top) and for MgO nanocrystals (bottom), as a function of the number N of ZnO or MgO units in the nanocrystal. In each case, the total energy of the nanocrystal was calculated for three different crystal structures: the rocksalt (RS), wurtzite (WZ), and zinc blende (ZB) phases.

$E_{tot}(N)$ is shown for ZnO and MgO. As expected, at high N, WZ and RS are the most stable structures for ZnO and MgO, respectively. MgO is, in fact, RS for all values of N. On the other hand, WZ ZnO becomes less stable than RS for $N < 218$. Thus, surprisingly, RS ZnO particles are stable without Mg addition for particles less than 1.6 nm in length. This size range roughly corresponds to the size range of the RS ZnO particles synthesized by Zou et al.[24] However, those particles were

coated with ionic surfactants, and the authors attributed the RS structure to the chemical environment of the particles. Our calculations, on the other hand, regard the intrinsic stability of the naked RS ZnO particles and do not consider any surfactants, and therefore, one should be cautious when comparing their experiments with our calculations.

Stability of Mixed $Mg_xZn_{1-x}O$ Nanocrystals. For the mixed $Mg_xZn_{1-x}O$ nanocrystals, it is not a priori clear which crystal structure the nanoparticles will have for $x < 0.67$, as there are two opposing contributions to the total energy of the particles: The bulk term will be minimal when the particle is in the WZ structure, whereas the surface term will be minimal when it is in the RS structure.

Assuming ZnO-terminated particles, plots such as that in Figure 8 can be made for any x by using the results of the bulk calculations on $Mg_xZn_{1-x}O$ as input for E_{bulk} and the ZnO surface energy calculations for E_S in eq 7. By finding the intersections of the RS and WZ curves, one can determine the maximum size for which the $Mg_xZn_{1-x}O$ rock salt particles are stable as a function of the composition. This is shown in Figure 9.
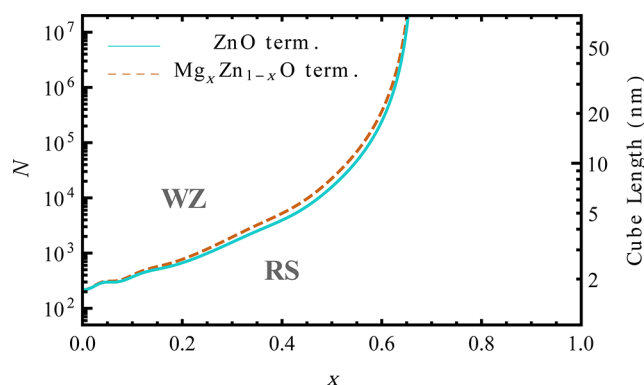
**Figure 9.** Maximum size of $Mg_xZn_{1-x}O$ nanoparticles for which RS is the most stable structure, when phase separation is not taken into account.

Instead of comparing only mixed phases of $Mg_xZn_{1-x}O$ for the three crystal structures, it is more physically relevant to compare them to a system of phase-separated WZ Zn-rich particles and RS Mg-rich particles. This system reduces to the WZ $Mg_xZn_{1-x}O$ system at $x = 0$ and to the RS $Mg_xZn_{1-x}O$ system at $x = 1$. The surfaces of the phase-separated system were assumed to be of the same composition as the bulk of the particles, and the surface energy was approximated by a linear interpolation of the MgO and ZnO surface energies.

Because RS ZnO layers have been grown on MgO substrates, a third options also comes to mind: a ZnO-terminated RS particle with a Zn-rich shell and a Mg-rich core. This last structure might be possible as a compromise between the competing effects of surface energy and phase separation. The very small lattice mismatch of 0.6% between RS MgO and RS ZnO suggests that this could be a favorable configuration. The surfaces of the core−shell particles, as well as of the $Mg_xZn_{1-x}O$ particles, were assumed to be completely ZnO, if allowed by size and composition. For small N and high x, the number of Zn atoms might not be large enough to cover the surface. This effect was taken into account, if necessary, by taking the fraction of the surface that could not be covered by ZnO to be MgO and adjusting the surface energy accordingly. Note that, in the

regimes where no phase separation occurs for the bulk, this particle reduces to the mixed-phase RS $Mg_xZn_{1-x}O$ particle. We did not consider similar constructions for other crystal structures, as we expect these to be unfavorable.

To test whether the core−shell particle could be a favorable construction, the interface energy between (001) RS MgO and (001) RS ZnO was also calculated, in a manner similar to the calculation of the surface energies. The supercell used is shown in Figure S5d (Supporting Information) and consisted of a (001) RS ZnO slab (four unit cells) stacked on a (001) RS MgO slab (four unit cells), without a vacuum. Because this interface energy is very small, the reference energies for pure MgO and pure ZnO were calculated using $1 \times 1 \times 8$ supercells to mimimize errors due to different cell sizes and k-meshes. The result, $\gamma_{interface} = -0.009$ J/m^2, is on the order of our numerical error. Therefore, the calculations predict that the formation energy of an RS ZnO/MgO interface is almost zero, likely because of the very low lattice mismatch and similar ionic radii of Mg and Zn.

In Figure 10, the RS $Mg_xZn_{1-x}O$ structure and the RS core−shell particle are shown schematically.
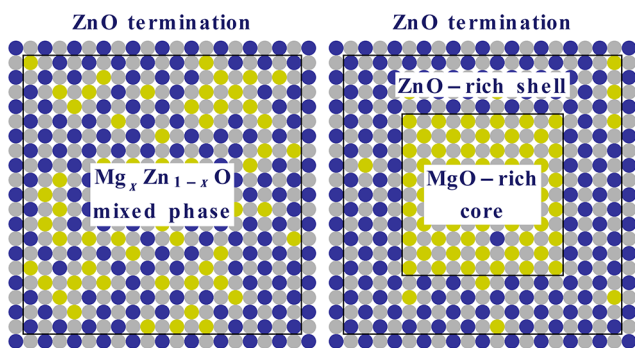
Figure 10. Two possible nanocrystal configurations. Left: RS $Mg_xZn_{1-x}O$ particle with ZnO-terminated surface. Right: MgO rich core with the RS structure forces the surrounding ZnO-rich shell into the RS phase. It is purely ZnO-terminated.

We compared the energies of the following configurations:

- an RS $Mg_xZn_{1-x}O$ particle, size N, ZnO-terminated;
- a WZ $Mg_xZn_{1-x}O$ particle, size N, ZnO-terminated;
- a ZB $Mg_xZn_{1-x}O$ particle, size N, ZnO-terminated;
- a phase-separated system, with a weighted average of a Zn-rich WZ particle and a Mg-rich RS particle, each of size N, and with a surface composition similar to that of the bulk; and
- a core−shell particle, size N, with an Mg-rich RS core, Zn-rich RS shell, and ZnO-terminated surface.

Comparison of all of these energies then gives the size−composition phase diagrams shown in Figure 11. At 0 K, the RS phase is the most stable crystal structure for low N, whereas phase separation is preferred at $N \gtrsim 5 \times 10^2$. Core−shell morphologies are predicted in three narrow ranges; however, the differences between the energy of an RS $Mg_xZn_{1-x}O$ and a core−shell particle are often very small (1−10 meV/fu), indicating that the two configurations might both form in these regions of the phase diagram.

At elevated temperature, the energy differences between these configurations increase, because of the effect of configurational entropy. The WZ and RS $Mg_xZn_{1-x}O$ phases become stable for the bulk at low and high x, respectively, and
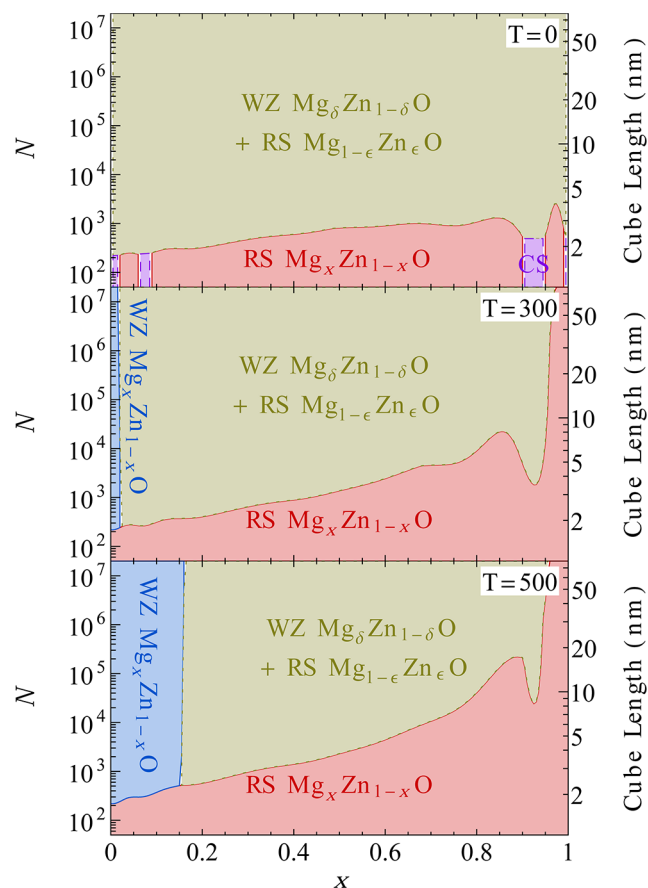
Figure 11. Size−composition ($N−x$) phase diagram. ZnO-terminated WZ and RS $Mg_xZn_{1-x}O$ particles are compared with a phase-separated system of ZnO-rich WZ particles and MgO-rich RS particles and with the core−shell particle described in the text. Red denotes the stable RS $Mg_xZn_{1-x}O$ region, blue denotes the stable WZ $Mg_xZn_{1-x}O$ region, green denotes the phase-separated region of ZnO-rich WZ and MgO-rich RS particles, and purple (for $T = 0$) denotes the region where core−shell (CS) particles are stable.

in between, the RS $Mg_xZn_{1-x}O$ phase is stable for higher N than at $T = 0$ K. Please note that the core−shell model is predicted to be stable only at very low temperatures. Whereas the bulk phase diagram (Figure 3) could not explain the results found by Limpijumnong et al.,[33] Figure 11 is in better agreement with their results. Because of the stabilizing effect of surface energies, Zn is much better miscible in RS MgO than Mg is in WZ ZnO. This shows that, at the nanoscale, the combination of formation energy, configurational entropy, and surface energy can explain the formation of rock salt Mg-doped ZnO nanocrystals.

■ CONCLUSIONS

In summary, the relative stability of $Mg_xZn_{1-x}O$ phases in the wurtzite and rock salt crystal structures was investigated by means of DFT total energy calculations. Lattice parameters and Bader charges were determined. As a result, we showed that the rock salt phase is energetically favored over the wurtzite phase for Mg concentrations of $x > 0.67$. The phase diagram (Figure 3), obtained by taking only "ideal" mixing entropies into account, indicates that ZnO and MgO are only slightly miscible up to temperatures of several hundred kelvin and that, in general, phase separation will occur for the bulk phases. Therefore, the formation of Mg-doped ZnO nanocrystals in the

rock salt structure cannot be explained solely by bulk formation energies.

A breakthrough in understanding comes from surface energy calculations, which show that ZnO surfaces are always lower in energy than their MgO counterparts. This implies that $Mg_xZn_{1-x}O$ nanoparticles are ZnO-terminated. Surprisingly, the ZnO rock salt (001) surface energy is lowest of all, low enough to stabilize very small pure ZnO rock salt nanoparticles (less than 1.6 nm). At finite temperature, Mg addition greatly extends the size range for which these rock salt particles are stable.

At $T = 0$, the phase diagram shows regimes in which a core–shell particle is the most stable configuration, although the energy differences with mixed phases are very small. Nonetheless, it is clear that the core–shell morphology of heterogeneous nanocrystals is a result of phase separation at the nanoscale and depends also on mixing energies and surface energies. The framework presented herein provides a means to predict whether core–shell or structure-dependent mixed-phase particles will be formed.

To fully understand the effective stabilization of semiconductor nanocrystals in unusual crystal structures by means of doping with extrinsic atoms, more experimental and simulation studies are needed, for example, taking entropy into account more accurately, including line energies, and considering effects that significantly affect surface properties, such as the presence of surfactants and a suspending liquid.

■ ASSOCIATED CONTENT

Ⓢ Supporting Information

Discussion of the dilute $Mg_xZn_{1-x}O$ phases, figures of lattice constants, figures of the supercells used in the calculations, figures of the DOS as a function of U and as a function of x, additional figures on the Bader charge distribution of several slabs, and a more detailed description of the functions used in determining the phase diagram (Figure 11). This material is available free of charge via the Internet at http://pubs.acs.org.

■ AUTHOR INFORMATION

Corresponding Authors
*E-mail: r.s.koster@uu.nl.
*E-mail: m.a.vanhuis@uu.nl.

Notes
The authors declare no competing financial interest.

■ ACKNOWLEDGMENTS

■ REFERENCES

(1) Pearton, S.; Norton, D.; Ip, K.; Heo, Y.; Steiner, T. Recent progress in processing and properties of ZnO. *Prog. Mater. Sci.* **2005**, *50*, 293–340.

(2) Schmidt-Mende, L.; MacManus-Driscoll, J. L. ZnO nanostructures, defects, and devices. *Mater. Today* **2007**, *10*, 40–48.

(3) Özgür, U.; Alivov, Y. I.; Liu, C.; Teke, A.; Reshchikov, M. A.; Doan, S.; Avrutin, V.; Cho, S.-J.; Morko, H. A comprehensive review of ZnO materials and devices. *J. Appl. Phys. (Melville, NY, U.S.)* **2005**, *98*, 041301.

(4) Djurii, A.; Leung, Y. H. Optical Properties of ZnO Nanostructures. *Small* **2006**, *2*, 944–961.

(5) Bagnall, D. M.; Chen, Y. F.; Zhu, Z.; Yao, T.; Koyama, S.; Shen, M. Y.; Goto, T. Optically pumped lasing of ZnO at room temperature. *Appl. Phys. Lett.* **1997**, *70*, 2230–2232.

(6) Fortunato, E.; Barquinha, P.; Pimentel, A.; Gonalves, A.; Marques, A.; Pereira, L.; Martins, R. Fully Transparent ZnO Thin-Film Transistor Produced at Room Temperature. *Adv. Mater.* **2005**, *17*, 590–594.

(7) Zhang, Q.; Dandeneau, C. S.; Zhou, X.; Cao, G. ZnO Nanostructures for Dye-Sensitized Solar Cells. *Adv. Mater.* **2009**, *21*, 4087–4108.

(8) Tsukazaki, A.; Ohtomo, A.; Onuma, T.; Ohtani, M.; Makino, T.; Sumiya, M.; Ohtani, K.; Chichibu, S. F.; Fuke, S.; Segawa, Y. Repeated temperature modulation epitaxy for p-type doping and light-emitting diode based on ZnO. *Nat. Mater.* **2005**, *4*, 42–46.

(9) Wan, Q.; Li, Q. H.; Chen, Y. J.; Wang, T. H.; He, X. L.; Li, J. P.; Lin, C. L. Fabrication and ethanol sensing characteristics of ZnO nanowire gas sensors. *Appl. Phys. Lett.* **2004**, *84*, 3654–3656.

(10) Soci, C.; Zhang, A.; Xiang, B.; Dayeh, S. A.; Aplin, D. P. R.; Park, J.; Bao, X. Y.; Lo, Y. H.; Wang, D.; ZnO Nanowire, U. V. Photodetectors with High Internal Gain. *Nano Lett.* **2007**, *7*, 1003–1009.

(11) Dai, Y.; Zhang, Y.; Li, Q.; Nan, C. Synthesis and optical properties of tetrapod-like zinc oxide nanorods. *Chem. Phys. Lett.* **2002**, *358*, 83–86.

(12) Yang, Y.; Jin, Y.; He, H.; Wang, Q.; Tu, Y.; Lu, H.; Ye, Z. Dopant-Induced Shape Evolution of Colloidal Nanocrystals: The Case of Zinc Oxide. *J. Am. Chem. Soc.* **2010**, *132*, 13381–13394.

(13) Ding, Y.; Wang, Z. L.; Sun, T.; Qiu, J. Zinc-Blende ZnO and Its Role in Nucleating Wurtzite Tetrapods and Twinned Nanowires. *Appl. Phys. Lett.* **2007**, *90*, 153510.

(14) Heo, Y. W.; Kaufman, M.; Pruessner, K.; Siebein, K. N.; Norton, D. P.; Ren, F. ZnO/Cubic (Mg,Zn)O Radial Nanowire Heterostructures. *Appl. Phys. A: Mater. Sci. Process* **2005**, *80*, 263–266.

(15) Rosenberg, R. A.; Shenoy, G. K.; Chisholm, M. F.; Tien, L.; Norton, D.; Pearton, S. Getting to the Core of the Problem: Origin of the Luminescence from (Mg,Zn)O Heterostructured Nanowires. *Nano Lett.* **2007**, *7*, 1521–1525.

(16) Kong, X. Y.; Wang, Z. L. Spontaneous Polarization-Induced Nanohelixes, Nanosprings, and Nanorings of Piezoelectric Nanobelts. *Nano Lett.* **2003**, *3*, 1625–1631.

(17) Li, S.; Li, Z. W.; Tay, Y. Y.; Armellin, J.; Gao, W. Growth Mechanism and Photonic Behaviours of Nanoporous ZnO Microcheerios. *Cryst. Growth Des.* **2008**, *8*, 1623–1627.

(18) Duzynska, A.; Hrubiak, R.; Drozd, V.; Teisseyre, H.; Paszkowicz, W.; Reszka, A.; Kaminska, A.; Saxena, S.; Fidelus, J. D.; Grabis, J. The Structural and Optical Properties of ZnO Bulk and Nanocrystals under High Pressure. *High Pressure Res.* **2012**, *32*, 354–363.

(19) Hou, D.; Ma, Y.; Gao, C.; Chaudhuri, J.; Lee, R. G.; Yang, H. Compression of a crystalline ZnO nanotube: An experimental exploration of the B4 to B1 transition mechanism. *J. Appl. Phys. (Melville, NY, U.S.)* **2009**, *105*, 104317.

(20) Baranov, A. N.; Sokolov, P. S.; Tafeenko, V. A.; Lathe, C.; Zubavichus, Y. V.; Veligzhanin, A. A.; Chukichev, M. V.; Solozhenko, V. L. Nanocrystallinity as a Route to Metastable Phases: Rock Salt ZnO. *Chem. Mater.* **2013**, *25*, 1775–1782.

(21) Jaffe, J. E.; Snyder, J. A.; Lin, Z.; Hess, A. C. LDA GGA Calculations for High-Pressure Phase Transitions in ZnO and MgO. *Phys. Rev. B: Condens. Matter Mater. Phys.* **2000**, *62*, 1660–1665.

(22) Pu, C. Y.; Tang, X.; Zhang, Q. Y. First Principles Study on the Structural and Optical Properties of the High-Pressure ZnO Phases. *Solid State Commun.* **2011**, *151*, 1533–1536.

(23) Saeed, Y.; Shaukat, A.; Ikram, N.; Tanveer, M. Structural and Electronic Properties of Rock Salt Phase of ZnO under Compression. *J. Phys. Chem. Solids* **2008**, *69*, 1676–1683.

(24) Zou, B. S.; Volkov, V. V.; Wang, Z. L. Optical Properties of Amorphous ZnO, CdO, and PbO Nanoclusters in Solution. *Chem. Mater.* **1999**, *11*, 3037–3043.

(25) Zhang, Y.; Gao, Z.; Gu, Y. First-Principles Studies on the Structural Transition of ZnO Nanowires at High Pressure. *J. Nanomater.* **2010**, *2010*, 462032.

(26) Wang, Y.; Hou, T.; Tian, S.; Lee, S.; Li, Y. Influence of doping effect on zinc oxide by first-principles studies. *J. Phys. Chem. C* **2011**, *115*, 7706–7716.

(27) Bobade, S. M.; Choo, S. M.; Lee, K.; Park, S.; Park, G.; Shin, K.; Jung, M.-H. A Reconstruction of Cubic rs-ZnO on MgO (200) Substrate through (100) Plane of w-ZnO:rs-ZnO for Transparent Electronic Application. *Appl. Phys. Lett.* **2012**, *100*, 072102.

(28) Yuan, H. T.; Liu, Y. Z.; Mei, Z. X.; Zeng, Z. Q.; Guo, Y.; Du, X. L.; Jia, J. F.; Zhang, Z.; Xue, Q. K. Metastable Rocksalt ZnO Interfacial Layer and Its Influence on Polarity Selection of Zn-Polar ZnO Films. *J. Cryst. Growth* **2010**, *312*, 263–266.

(29) Yan, X.; Gu, Y.; Zhang, X.; Huang, Y.; Qi, J.; Zhang, Y.; Fujita, T.; Chen, M. Doping Effect on High-Pressure Structural Stability of ZnO Nanowires. *J. Phys. Chem. C* **2009**, *113*, 1164–1167.

(30) Ueda, K.; Tabata, H.; Kawai, T. Magnetic and electric properties of transition-metal-doped ZnO films. *Appl. Phys. Lett.* **2001**, *79*, 988–990.

(31) Chen, N. B.; Wu, H. Z.; Qiu, D. J.; Xu, T. N.; Chen, J.; Shen, W. Z. Temperature-Dependent Optical Properties of Hexagonal and Cubic $Mg_xZn_{1-x}O$ Thin-Film Alloys. *J. Phys.: Condens. Matter* **2004**, *16*, 2973–2980.

(32) Chen, J.; Zhen, W. Z.; Chen, N. B.; Qiu, D. J.; Wu, H. Z. The study of composition non-uniformity in ternary $Mg_xZn_{1-x}O$ thin films. *J. Phys.: Condens. Matter* **2003**, *15*, L475–L482.

(33) Limpijumnong, S.; Jutimoosik, J.; Palakawong, N.; Klysubun, W.; Nukeaw, J.; Du, M.-H.; Rujirawat, S. Determination of Miscibility in MgO−ZnO Nanocrystal Alloys by X-ray Absorption Spectroscopy. *Appl. Phys. Lett.* **2011**, *99*, 261901.

(34) Bader, R. F. W. *Atoms in Molecules: A Quantum Theory*; Oxford University Press: Oxford, U.K., 1990.

(35) Kresse, G.; Furthmüller, J. Efficiency of Ab-Initio Total Energy Calculations for Metals and Semiconductors Using a Plane-Wave Basis Set. *Comput. Mater. Sci.* **1996**, *6*, 15–50.

(36) Hohenberg, P.; Kohn, W. Inhomogeneous Electron Gas. *Phys. Rev.* **1964**, *136*, B864–B871.

(37) Kohn, W.; Sham, L. J. Self-Consistent Equations Including Exchange and Correlation Effects. *Phys. Rev.* **1965**, *140*, A1133–A1138.

(38) Kohn, W. Nobel Lecture: Electronic Structure of Matter—Wave Functions and Density Functional. *Rev. Mod. Phys.* **1999**, *71*, 1253–1266.

(39) Perdew, J. P.; Burke, K.; Ernzerhof, M. Generalized Gradient Approximation Made Simple. *Phys. Rev. Lett.* **1996**, *77*, 3865–3868.

(40) Kresse, G.; Joubert, D. From Ultrasoft Pseudopotentials to the Projector Augmented-Wave Method. *Phys. Rev. B: Condens. Matter Mater. Phys.* **1999**, *59*, 1758–1775.

(41) Blöchl, P. E. Projector Augmented-Wave Method. *Phys. Rev. B* **1994**, *50*, 17953–17979.

(42) Henkelman, G.; Arnaldsson, A.; Jónsson, H. A Fast and Robust Algorithm for Bader Decomposition of Charge Density. *Comput. Mater. Sci.* **2006**, *36*, 354–360.

(43) Sanville, E.; Kenny, S. D.; Smith, R.; Henkelman, G. Improved Grid-Based Algorithm for Bader Charge Allocation. *J. Comput. Chem.* **2007**, *28*, 899–908.

(44) Tang, W.; Sanville, E.; Henkelman, G. A Grid-Based Bader Analysis Algorithm Without Lattice Bias. *J. Phys.: Condens. Matter* **2009**, *21*, 084204.

(45) Van de Walle, C. G.; Neugebauer, J. First-principles calculations for defects and impurities: Applications to III-nitrides. *J. Appl. Phys.* **2004**, *95*, 3851–3879.

(46) Oba, F.; Togo, A.; Tanaka, I.; Paier, J.; Kresse, G. Defect energetics in ZnO: A hybrid Hartree-Fock density functional study. *Phys. Rev. B* **2008**, *77*, 245202.

(47) Liu, J. Z.; Zunger, A. Thermodynamic states and phase diagrams for bulk-incoherent, bulk-coherent, and epitaxially-coherent semiconductor alloys: Application to cubic (Ga,In)N. *Phys. Rev. B* **2008**, *77*, 205201.

(48) Kresse, G.; Dulub, O.; Diebold, U. Competing Stabilization Mechanism for the Polar ZnO(0001)-Zn Surface. *Phys. Rev. B* **2003**, *68*, 245409.

(49) Lauritsen, J. V.; Porsgaard, S.; Rasmussen, M. K.; Jensen, M. C. R.; Bechstein, R.; Meinander, K.; Clausen, B. S.; Helveg, S.; Wahl, R.; Kresse, G. Stabilization Principles for Polar Surfaces of ZnO. *ACS Nano* **2011**, *5*, 5987–5994.

(50) Spencer, M. J. S.; Wong, K. W. J.; Yarovsky, I. Density Functional Theory Modelling of ZnO ($10\bar{1}0$) and ZnO ($2\bar{1}\bar{1}0$) Surfaces: Structure, Properties and Adsorption of N2O. *Mater. Chem. Phys.* **2010**, *119*, 505–514.

(51) Cooke, D. J.; Marmier, A.; Parker, S. C. Surface Structure of ($10\bar{1}0$) and ($11\bar{2}0$) Surfaces of ZnO with Density Functional Theory and Atomistic Simulation. *J. Phys. Chem. B* **2006**, *110*, 7985–7991.

(52) Beltrán, A.; Andrés, J.; Calatayud, M.; Martins, J. B. L. Theoretical Study of ZnO ($10\bar{1}0$) and Cu/ZnO ($10\bar{1}0$) Surfaces. *Chem. Phys. Lett.* **2001**, *338*, 224–230.

(53) Marana, N. L.; Longo, V. M.; Longo, E.; Martins, J. B. L.; Sambrano, J. R. Electronic and Structural Properties of the ($10\bar{1}0$) and ($11\bar{2}0$) ZnO Surfaces. *J. Phys. Chem. A* **2008**, *112*, 8958–8963.

(54) Wander, A.; Schedin, F.; Steadman, P.; Norris, A.; McGrath, R.; Turner, T. S.; Thornton, G.; Harrison, N. M. Stability of Polar Oxide Surfaces. *Phys. Rev. Lett.* **2001**, *86*, 3811–3814.

(55) Broqvist, P.; Gronbeck, H.; Panas, I. Surface properties of alkaline earth metal oxides. *Surf. Sci.* **2004**, *554*, 262–271.

(56) Evarestov, R. A.; Bandura, A. V. HF and DFT Calculations of MgO Surface Energy and Electrostatic Potential Using Two- and Three-Periodic Models. *Int. J. Quantum Chem.* **2004**, *100*, 452–459.

(57) Wulff, G. Zur frage der geschwindigkeit des wachsturms under auflösung der kristallflächen. *Z. Kristallogr.* **1901**, *34*, 449–530.